

Novel family of topological semimetals with butterflylike nodal lines

Xiaoting Zhou^{1,*} Chuang-Han Hsu,² Hugo Aramberri¹, Mikel Iraola^{3,4}, Cheng-Yi Huang,^{5,1} Juan L. Mañes¹, Maia G. Vergniory,^{3,6} Hsin Lin⁵, and Nicholas Kioussis^{1,†}

¹Department of Physics and Astronomy, California State University, Northridge, California 91330, USA

²Department of Electrical and Computer Engineering, Faculty of Engineering, National University of Singapore, Singapore 117583

³Donostia International Physics Center, 20018 Donostia-San Sebastian, Spain

⁴Department of Condensed Matter Physics, University of the Basque Country UPV/EHU, Apartado 644, 48080 Bilbao, Spain

⁵Institute of Physics, Academia Sinica, Taipei 11529, Taiwan

⁶IKERBASQUE, Basque Foundation for Science, Maria Diaz de Haro 3, 48013 Bilbao, Spain



(Received 29 April 2020; revised 10 March 2021; accepted 13 September 2021; published 22 September 2021)

In recent years, the exotic properties of topological semimetals (TSMs) have attracted great attention and significant efforts have been made in seeking new topological phases and material realization. In this work, we propose a family of TSMs which harbors an unprecedented nodal line (NL) landscape consisting of a pair of concentric intersecting coplanar ellipses (CICEs) at half-filling. Meanwhile, the CICE at half-filling guarantees the presence of a second pair of CICEs beyond half-filling. Both CICEs are linked at fourfold degenerate points at zone boundaries. In addition, we identify the generic criteria for the existence of the CICE in a time-reversal-invariant *spinless* fermion system or a spinful system with negligible spin-orbital coupling. Consequently, 9 out of 230 space groups (SGs) are feasible for hosting CICEs whose location centers in the first Brillouin zone (BZ) are identified. We provide a simple model with SG *Pbam* (No. 55) which exhibits CICEs, and the exotic intertwined drumhead surface states, induced by double band inversions. Finally, we propose a series of material candidates that host butterflylike CICE NLs, such as ZrX_2 ($X = P, As$), Tl_2GeTe_5 , CYB_2 , and Al_2Y_3 .

DOI: [10.1103/PhysRevB.104.125135](https://doi.org/10.1103/PhysRevB.104.125135)

I. INTRODUCTION

Topological semimetals (TSMs) [1–4] have emerged among the most active frontiers in condensed matter physics in recent years, drawing widespread attention from both the theoretical and the experimental communities. In the noninteracting limit, TSMs describe systems which are characterized by the topologically robust band-crossings manifolds between conduction and valence bands in momentum k space. These manifolds can be zero-dimensional (0D) nodal points, e.g., three-dimensional (3D) Weyl semimetals (WSMs) [4–6] and Dirac semimetals (DSMs) [4,7–11], and one-dimensional (1D) nodal lines/loops, e.g., nodal-line semimetals (NLSMs) [2,12]. Around these band crossings, electron excitations behave drastically differently from the conventional Schrödinger fermions in normal metals. For example, the low-energy electrons in 3D DSMs and WSMs resemble the relativistic Dirac and Weyl fermions, making it possible to mimic high-energy physics phenomena. Meanwhile, TSMs are distinguished from normal semimetals by the accompanying topological indices due to the aforementioned manifolds. Moreover, because of these unique electronic features, TSMs present exotic properties in different ways, such as Fermi arcs [13] and drumhead surface states (SSs) [14] on surfaces of WSMs and

NLSMs, respectively, and novel transport phenomena e.g., the negative magnetoresistance related to the chiral anomaly in both Weyl and Dirac SMs [15–17].

Among TSMs, NLSMs possess the highest variability. Nodal lines (NLs) can be integrated in various configurations, e.g., a chain link [11,18–20], a Hopf link [19], and a knot [21], where each of them carries its unique topology. Since the essential characteristics, band crossings, of various TSMs are mostly protected by crystalline symmetries, a thorough classification of a particular type of TSMs in all space groups can greatly accelerate the experimental discovery. There exist well-established classifications for DSMs and WSMs [22–24], and the triple point semimetals [25]. However, for most types of NLSMs proposed today, except the chain link [18] and some types of intersecting rings [26], the symmetry criteria of the emergence of particular nodal lines remain deficient.

In this paper, we introduce a type of NLSM in time-reversal-invariant *spinless* systems, which hosts a butterflylike nodal line (NL) consisting of a pair of concentric intersecting coplanar ellipses (CICEs) at half-filling residing on a plane in k space, as indicated by the blue and red concentric ellipses in Fig. 1(a). Meanwhile, the half-filling CICE consequently guarantees the presence of another pair of CICEs formed by band crossings beyond half-filling, which is indicated by the magenta lines in Fig. 1(b). We demonstrate that CICEs can be sustained by nonsymmorphic crystalline symmetries including two glide symmetries, and only nine space groups

*physxtzhou@gmail.com

†nick.kioussis@csun.edu

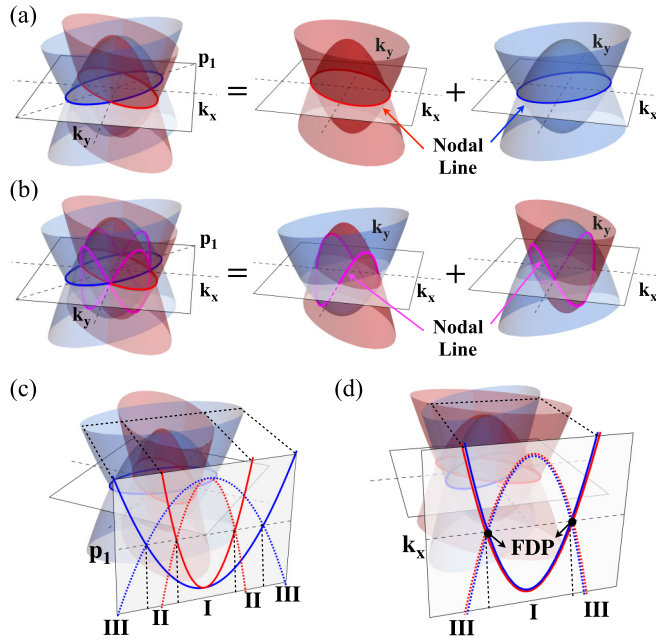


FIG. 1. Schematic band structures showing the mechanism of the formation of the CICE NLs, resulting from the DBI. (a) The half-filling CICE can be decomposed into two ellipses in red and blue, respectively, which are locked by symmetries. Each ellipse is the band crossing due to a single band inversion and protected by mirror (or glide) symmetry \mathcal{M}_z (or \mathcal{G}_z). (b) The second pair of CICE NLs (labeled in magenta) emerge due to the crossings between the bands denoted in red and blue corresponding to crossings between two occupied (one-quarter filling) or two unoccupied (three-quarter filling) bands. These cross the Fermi surface (FS) leading to the intersection of four NLs at four points on the k_x and k_y axes. Band structures along the paths (c) p_1 and (d) the k_x axis. The bands labeled by solid and dashed lines carry different eigenvalues of \mathcal{M}_z (or \mathcal{G}_z), and opposite parity at the center TRIM point of the CICE. Bands are doubly degenerate along the k_x axis (d) and similarly, along the k_y axis. I, II, and III denote the regions divided by the NLs.

(SGs) are feasible to host it. These SGs are classified into two categories by their point group symmetries, which are D_{2h} and D_{4h} . Moreover, we provide a tight-binding model for one of the SGs, *Pbam* (No. 55), which exhibits CICEs and hosts exotic intertwined drumhead surface states. In the end, five material candidates from these two categories, hosting the proposed CICEs, are suggested for further experimental studies, such as time-resolved angle-resolved photoemission spectroscopy and studies of magneto-optical effects [27,28].

II. SYMMETRY CRITERIA AND SPACE GROUPS

Conceptually, a pair of CICEs can be constructed by integrating two NL fermions. As shown in Fig. 1(a), CICEs denoted by the intersection of the red and blue ellipses on the $k_z = 0$ plane can be decomposed into two individual NL fermions. Each NL, the accidental twofold band crossings due to the band inversion, is further validated by the inherent crystal symmetry belonging to its parent bands, which is the mirror (or glide) reflection symmetry, $\mathcal{M}_z(\mathcal{G}_z) : (k_x, k_y, k_z) \rightarrow (k_x, k_y, -k_z)$. On the $k_z = 0$ plane, states [labeled by solid and

dashed lines in Fig. 1(c)] carrying different mirror (or glide) eigenvalues forbid their mutual hybridization, thus supporting the NL fermion. Since at each k point $\mathcal{M}_z(\mathcal{G}_z)$ only supplies two different eigenvalues, additional symmetry constraints along the k_x and k_y axes are demanded to sustain the fourfold degenerate points (FDPs) on the CICEs, i.e., the intersecting points of the two NL fermions, marked in Fig. 1(d).

Therefore, the additional symmetries required along k_x and k_y to guarantee the twofold degeneracy can be realized by introducing an antiunitary symmetry, $\mathcal{T}\mathcal{Q}$, which combines time-reversal symmetry (TRS) \mathcal{T} and a spatial symmetry \mathcal{Q} . Thus, the Kramer-like twofold degeneracy is enforced at $\mathcal{T}\mathcal{Q}$ -invariant points where $(\mathcal{T}\mathcal{Q})^2 = -1$. For a spinless system, $\mathcal{T}^2 = +1$, which in turn requires that \mathcal{Q} is a nonsymmorphic symmetry, with eigenvalues of $\pm i$ [9,29] at certain points on the boundaries of the Brillouin zone (BZ). Consequently, the qualified candidates of \mathcal{Q} for ensuring the degeneracy on the k_x (k_y) are \mathcal{G}_x or \mathcal{S}_y (\mathcal{G}_y or \mathcal{S}_x), so the CICE should be centered at $(\pi, \pi, 0$ or $\pi)$. Here, $\mathcal{S}_{x(y)} = \{\mathcal{C}_{2x(2y)}|\mathbf{t}_{x(y)}\}$ denotes a twofold screw rotation with respect to the $k_{x(y)}$ axis accompanied by a translation $\mathbf{t}_{x(y)} = \frac{1}{2}\hat{x}(\hat{y})$, and $\mathcal{G}_{x(y)} = \{\mathcal{M}_{x(y)}|\mathbf{t}_{y(x)}\}$ is a glide symmetry normal to $k_{x(y)}$, which contains a fractional translation $\mathbf{t}_{y(x)} = \frac{1}{2}\hat{y}(\hat{x})$. To avoid replicas of CICEs on other symmetry-related planes, n -fold rotation and rotoinversion symmetries with $n > 2$ with respect to the $k_{x(y)}$ axes are not allowed. In addition, each Kramer-paired state should carry the same mirror symmetry eigenvalue of \mathcal{M}_z (or \mathcal{G}_z). Furthermore, symmetry-enforced degeneracy is not allowed at any generic point of the $k_z = 0$ plane other than the $k_{x(y)}$ axis.

In summary, the criteria for generating CICEs in a spinless crystal preserving TRS include the following: (i) the little group of the center of the CICE is nonsymmorphic with corresponding point group (PG) D_{2h} or D_{4h} ; (ii) the crystal contains two glide $\mathcal{G}_{x(y)}$ or screw $\mathcal{S}_{y(x)}$ symmetries with respect to the axes lying on a mirror \mathcal{M}_z or a glide \mathcal{G}_z plane; and (iii) at the center of the CICE, \mathcal{M}_z (\mathcal{G}_z) should commute with other preserved and required symmetries. According to the above criteria, we have exhaustively scanned all 230 SGs, and determined 9 possible SGs to host CICEs. The corresponding positions of the center of the CICE and the corresponding axes of \mathcal{S} or \mathcal{G} are listed in Table I.

TABLE I. List of space groups (SGs) and corresponding point groups (PGs) that can host CICEs. We also list the possible positions of the CICE centers and the axes on which the fourfold degenerate points on the CICE emerge

PGs	SGs (No.)	Positions	Axes
D_{2h}	<i>Pbam</i> (55)	$(\pi, \pi, 0), (\pi, \pi, \pi)$	$\{[100], [010]\}$
	<i>Pccn</i> (56)	(π, π, π)	
	<i>Pnnm</i> (58)	$(\pi, \pi, 0)$	
	<i>Pnma</i> (62)	$(\pi, 0, \pi)$	$\{[100], [001]\}$
D_{4h}	<i>P4/mmb</i> (127)	$(\pi, \pi, 0), (\pi, \pi, \pi)$	$\{[100], [010]\}$
	<i>P4/mnc</i> (128)	$(\pi, \pi, 0)$	
	<i>P4₂/mbc</i> (135)	$(\pi, \pi, 0)$	
	<i>P4₂/mnm</i> (136)	$(\pi, \pi, 0)$	
	<i>P4₂/ncm</i> (138)	(π, π, π)	

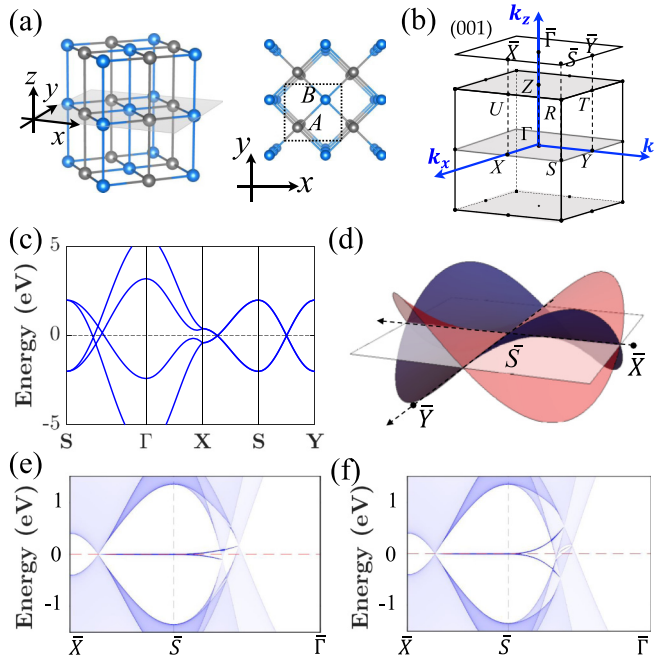


FIG. 2. (a) Orthorhombic crystal structure of the lattice model in Eq. (1) in SG *Pbam*, consisting of a bipartite lattice with two sublattices *A* (in blue) and *B* (in gray). (b) Bulk BZ, the projected (001) surface BZ, and high-symmetry points. (c) Band structures of the model without spin-orbit coupling. (d) Schematic dispersion of the drumhead surface states (DSSs) of the (001) surface stemming from the NLs, with two saddlelike hyperbolic paraboloids intertwined with each other. (e), (f) Dispersion along high symmetric directions of two types of DSSs on the (001) surface. (e) Type-I DSSs stem from the CICE FS, while (f) type II from the NLs labeled in magenta in Fig. 1(b).

III. LATTICE MODEL AND SURFACE STATES

To validate the criteria derived above and explore the underlying topology of CICEs, we construct a minimal four-band tight-binding lattice model for the SG *Pbam* (No. 55). The minimal required symmetries are $\mathcal{M}_z = \{m_{001}|000\}$, $\mathcal{G}_x = \{m_{100}|\frac{1}{2}\frac{1}{2}0\}$, and $\mathcal{G}_y = \{m_{010}|\frac{1}{2}\frac{1}{2}0\}$. The model is a bipartite lattice, where the sublattices denoted by *A* (gray) and *B* (blue) occupy the $2a$ Wyckoff position at $\mathbf{r}_A = (0, 0, 0)$ and $\mathbf{r}_B = (\frac{1}{2}, \frac{1}{2}, 0)$ in a unit cell [see Fig. 2(a) for the structure]. Each sublattice contains two orbitals, p_z and d_{xy} , described by the Pauli matrix σ , and τ for the *A* and *B* sublattices (see Appendix A for details). For a spinless system, employing the basis $\Psi = (p_z^A, d_{xy}^A, p_z^B, d_{xy}^B)^T$ the symmetry-constrained tight-binding Hamiltonian is of the form

$$H_0(\mathbf{k}) = [(\alpha \cos k_x + \beta \cos k_y + \gamma \cos k_z) + \delta_0] \tau_0 \sigma_3 + \cos \frac{k_x}{2} \cos \frac{k_y}{2} \cos k_z (\lambda_{10} \tau_1 \sigma_0 + \lambda_{13} \tau_1 \sigma_3)$$

satisfy the following conditions:

$$+ \sin k_z (\lambda_{32} \tau_3 \sigma_2) + \sin \frac{k_x}{2} \sin \frac{k_y}{2} \sin k_z (\lambda_{12} \tau_1 \sigma_2), \quad (1)$$

where α , β , γ , δ_0 , and λ_{ij} are constants.

Since the CICE can emerge on the mirror plane [gray shaded area in Fig. 2(b)] centered at the high-symmetry k point $S = (\pi, \pi, 0)$ [$R = (\pi, \pi, \pi)$] [Fig. 2(b)], we derive the effective $\mathbf{k} \cdot \mathbf{p}$ Hamiltonian around the $S(R)$ point,

$$H_{S(R)}(\mathbf{q}) = \frac{1}{2} (\alpha q_x^2 + \beta q_y^2 \mp \gamma q_z^2 + 2\delta_{S(R)} \tau_0 \sigma_3 + \frac{1}{4} q_x q_y (\lambda_{10} \tau_1 \sigma_0 + \lambda_{13} \tau_1 \sigma_3) + q_z (\lambda_{12} \tau_1 \sigma_2 + \lambda_{32} \tau_3 \sigma_2). \quad (2)$$

At $q_z = 0$, the Hamiltonian is diagonalized as $E_{S(R)}(q_x, q_y, 0) = \text{diag}(E_+^{A+B}, E_+^{A+B}, E_+^{A-B}, E_-^{A-B})$ on the basis $\Psi' = (p_z^{A+B}, d_{xy}^{A+B}, p_z^{A-B}, d_{xy}^{A-B})^T$, where $|\varphi^{A\pm B}\rangle = \frac{1}{\sqrt{2}}(|\varphi^A\rangle \pm |\varphi^B\rangle)$ ($\varphi = p_z, d_{xy}$) denote the bonding/antibonding states of the relevant orbitals. Each ellipse in the half-filling CICE is the line crossing between the conduction band and the valence band, which is referred to as type-I NL. Whereas, type-II NLs are the crossings between two conduction or two valence bands. If $|\lambda_{13}| > |\lambda_{10}|$, the crossings between the bands E_+^{A+B} (E_+^{A-B}) and E_-^{A+B} (E_-^{A-B}) give rise to the type-I NL, while E_+^{A+B} (E_+^{A-B}) and E_-^{A-B} (E_-^{A+B}) give rise to the type-II NLs. Otherwise, if $|\lambda_{13}| < |\lambda_{10}|$, type-I NLs evolve to type II, and vice versa. Thus, the corresponding NLs for the half-filling CICE can be obtained by solving the equations

$$|\lambda_{13}| > |\lambda_{10}| : \alpha q_x^2 + \beta q_y^2 \pm \frac{1}{2} \lambda_{13} q_x q_y + 2\delta_{S(R)} = 0, \\ |\lambda_{13}| < |\lambda_{10}| : \alpha q_x^2 + \beta q_y^2 \pm \frac{1}{2} \lambda_{10} q_x q_y + 2\delta_{S(R)} = 0. \quad (3)$$

After further analyses, we find that when the condition

$$\{\alpha \delta_{S(R)} < 0 \cap \alpha \beta > 0 \cap \alpha \neq \beta\} \quad (4)$$

is satisfied, where $\delta_{S,R} = \delta_0 - (\alpha + \beta \mp \gamma)$, the terms in the first line of Eq. (1) describe two concentric elliptic NLs with double band inversions at the S (R) point [Fig. 1(d)]. The terms in the second line in Eq. (1) adjust the anisotropy of each NL, resulting in two twisted elliptic NLs [see dispersion along $k_x = k_y$ in Fig. 2(c), where the band width differs in the two original elliptic NLs]. The angles of the elliptic NLs with respect to the k_x axis are determined via $\theta_{\pm} = \pm \frac{1}{2} \arctan \frac{\lambda}{2(\alpha - \beta)}$, where $\lambda = \max\{|\lambda_{10}|, |\lambda_{13}|\}$.

To explore the unique topological properties of the CICE NL, the system is designed to host CICEs centered at the S point and to have no additional band inversions at other time-reversal-invariant momentum points (TRIM). Thus, in addition to Eq. (4), the model parameters should be tuned to

$$\{\delta_S < 0 \cap \delta_R > 0 \cap \delta_{\Gamma} > \max(|\lambda_{10}|, |\lambda_{13}|) \cap \delta_Z > \max(|\lambda_{10}|, |\lambda_{13}|)\};$$

or

$$\{\delta_S > 0 \cap \delta_R < 0 \cap \delta_{\Gamma} < \min(-|\lambda_{10}|, -|\lambda_{13}|) \cap \delta_Z < \min(-|\lambda_{10}|, -|\lambda_{13}|)\}, \quad (5)$$

where $\delta_{\Gamma,Z} = \delta_0 + (\alpha + \beta \pm \gamma)$. The corresponding band structure is shown in Fig. 2(c), in which the distinctive features of CICEs can be recognized by comparing the bands along $S-\Gamma$ and $S-X$ (or $S-Y$). Since CICEs are comprised of two NLs, and the essential \mathcal{G}_x and \mathcal{G}_y symmetries are preserved on (001) surface, which is stabilized by the two-dimensional (2D) wallpaper group $P2gg$, we anticipate to observe two intertwined drumhead surface states (DSSs) [12]. At the \bar{S} point, $\mathcal{T} = \mathcal{K}$, and \mathcal{T} should commute with all spatial symmetries. Since both \mathcal{G}_x and \mathcal{G}_y should take the eigenvalues $\pm i$, the symmetry constraints can be determined as $\mathcal{G}_x = i\mu_2$, $\mathcal{G}_y = i\mu_2$, where $\mu_{1,2,3}$ are Pauli matrices acting in orbital space. The DSS, shown schematically in Fig. 2(d), can be described by the $\mathbf{k} \cdot \mathbf{p}$ Hamiltonian around the \bar{S} point,

$$H_{\text{DSS}}(q_x, q_y) = q_x q_y (a_3 \mu_3 + a_1 \mu_1), \quad (6)$$

where $a_{1,3}$ are real constants. Two saddlelike hyperbolic paraboloids [red and gray surfaces in Fig. 2(d)] are intertwined with each other, resulting in the doubly degenerate bands along $\bar{S}-\bar{X}$ and $\bar{S}-\bar{Y}$, respectively, which are enforced by \mathcal{G}_x and \mathcal{G}_y symmetries combined with \mathcal{T} . We would like to emphasize that these remarkable features exhibited by the new DSSs allow them to provide a great platform for studies of exotic emergent phenomena.

The calculated (001) surface band structure along $\bar{X}-\bar{S}-\bar{\Gamma}$ for $|\lambda_{10}| < |\lambda_{13}|$ is shown in Fig. 2(e). Intriguingly, we notice that another type of DSSs, shown in Fig. 2(f), can be realized when $|\lambda_{10}| > |\lambda_{13}|$ with all remaining parameters unchanged. We refer to the two different types of DSSs as type I/type II for the former/latter case. Type-II DSSs can be comprehended from the way one proceeds to decompose the second pair of CICEs into two single NLs. As shown in Fig. 1(b) the NLs (shown by magenta color) are allowed by the same band configurations with swapped conduction bands in comparison to the configurations of Fig. 1(a). In contrast to the NLs of the half-filling CICE, the NLs labeled in magenta are due to the crossings between two occupied bands (one-quarter filling) and two unoccupied bands (three-quarter filling), respectively, and hence might be irrelevant for electron excitation at a half-filling system. However, the CICE TSM introduces another possibility. As one cannot distinguish whether the FDPs of CICEs belong to the half-filling CICE or the second pair of CICEs, both of them can provide topological DSSs on an equal footing due to the inherent band inversion. Even though both types of NL contribute to the DSS on the (001) surface, \mathcal{G}_x and \mathcal{G}_y permit solely one pair of DSSs, forcing in turn the other pair to merge into the bulk states. Consequently, the DSS of CICE-NL in the spinless case may appear in either way depending on the coupling parameter details.

IV. MATERIAL CANDIDATES

We propose a series of compounds as material candidates for the experimental realization of this type of TSMs that host butterflylike CICE NLs, such as ZrX_2 ($X = \text{As}, \text{P}$) with CICEs centered at TRIM point U ($\pi, \pi, 0$), as well as TL_2GeTe_5 , CYB_2 , and Al_2Y_3 at M ($\pi, \pi, 0$), respectively. Here we take the ZrAs_2 and TL_2GeTe_5 as representatives. The equilibrium

lattice constants and electronic structure of both compounds were determined by first-principles density functional theory (DFT) calculations using the VASP [30] and WIEN2K [31] packages. CYB_2 and Al_2Y_3 were found using the *Advanced Search Tools* [32–36] (see Appendix C for details).

The crystal structure of ZrAs_2 is orthorhombic with SG $Pnma$ (No. 62) and is displayed in Fig. 3(a). The calculated lattice parameters $a = 6.847 \text{ \AA}$, $b = 3.718 \text{ \AA}$, and $c = 9.123 \text{ \AA}$ are in agreement with the experimental ones [37,38]. The band structure without SOC close to the $U = (\pi, 0, \pi)$ point of the BZ is shown in Fig. 3(b) along two high-symmetry lines ($X-U$ and $U-\Gamma$). The second material, TL_2GeTe_5 , has tetragonal structure with SG $P4/mbm$ (No. 127) and the crystal structure is depicted in Fig. 3(d). In the DFT calculations the experimental structure of TL_2GeTe_5 [39,40] is applied, and the band structures along two essential high-symmetry k paths $M \rightarrow X$ and $M \rightarrow \Gamma$ are shown in Fig. 3(e), which reveal band crossings alike those observed in ZrAs_2 .

In order to corroborate the CICE NLs in ZrAs_2 around U we used the Bloch functions obtained with DFT to construct a Wannier-function based model employing the WANNIER90 package [41]. The model reproduces the bands around the Fermi level, allowing the scan of band crossings in the BZ more efficiently than direct DFT calculations. As shown in Fig. 3(c) the nodal points around the U point form a butterflylike CICE with a small energy dispersion. In the case of TL_2GeTe_5 , the band crossings, shown in Fig. 3(f), occur closer to the M point, yielding a smaller area enclosed by the CICE and a lower energy dispersion.

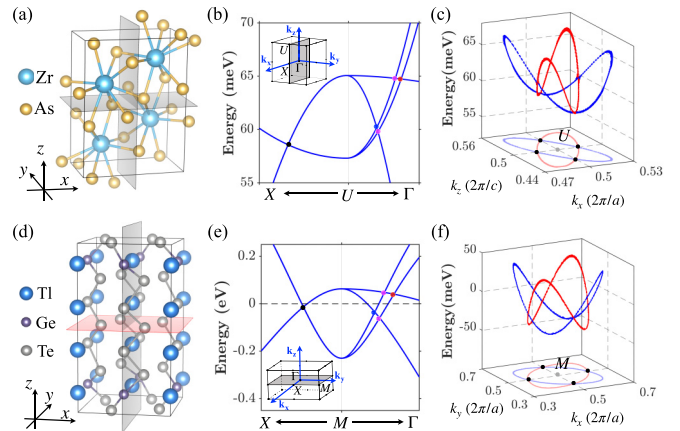


FIG. 3. Crystal structure of bulk (a) ZrAs_2 and (d) TL_2GeTe_5 . Band structure of (b) ZrAs_2 and (e) TL_2GeTe_5 close to the Fermi energy without spin-orbit coupling (SOC) along the symmetry lines in the BZ shown in the insets where high-symmetry points are marked. The relevant crossings on U (M)- Γ for the half-filling and the second pair of CICEs are indicated by [red, blue] and magenta dots, respectively. Energy-momentum spread for the half-filling CICE nodal lines in the BZ for (c) ZrAs_2 centered at the U point on the (010) plane (gray shaded) and (f) TL_2GeTe_5 at the M point on the (001) plane (gray shaded). The black dots shown on the projected CICEs in the k space are the FDPs and one of them is indicated in the band along $X-U$ (M) of (b) and (e). As suggested by the crossings in (b) and (e), the energy spreads for the second pair of CICEs are very similar.

V. CONCLUSION

In summary, we have proposed a type of TSMs which unveil intriguing butterflylike CICE NLs. We have derived the symmetry criteria to generate the CICE, identified the nine SGs which can host such complex NLs, and determined the positions of the CICE centers in the BZ for each SG. In one of the SGs, *Pbam* (No. 55), we have introduced a model of spinless fermions, which hosts CICEs and supports the intriguing two intertwined DSSs. We have also calculated the Zak phase, which is related to the bulk-boundary correspondence [42–49] (see details in Appendix B). In our following work [50], we have investigated the effect of SOC on a CICE TSM, where the connection of the CICE NLSM and the TCI protected by glide symmetries is revealed. More specifically, the intertwined DSSs evolve to topological surface states (TSSs) with fourfold Dirac fermion. In addition, a 3D higher-order topological insulator (HOTI) protected by glide symmetry emerges in the presence of SOC. The appearance of a pair of doubly degenerate saddle points or Van Hove singularities on the surface states, provides a platform for exploring the interplay between topological states and the physics of strongly correlated systems, e.g., the related interaction-driven instabilities, such as superconducting states and charge-density-wave (CDW) phase.

Finally, we have predicted candidate materials which can host such exotic NL landscapes. Many materials may have substantial SOC, which would lift the band crossings and drive the system to an insulating phase. However, for materials with negligible SOC, the band gaps lifted by SOC might be small. Hence, those observable physical properties, e.g., electronic transport, still hold. In addition, this model also can be realized in other spinless fermion systems, such as photonic crystals. In general, the study of the material band structures without SOC provides some clues and indicates the connections between a topological semimetal phase (without SOC) and a topological insulating phase (with SOC) [50]. We hope that these predictions will motivate experimental studies of such complex NLs. For instance, the optical and magneto-optical signatures of CICE nodal lines are worth investigating.

ACKNOWLEDGMENTS

The work at CSUN was supported by NSF-Partnership in Research and Education in Materials (PREM) Grant No.

DMR-1828019. The work of J.L.M. has been supported by Spanish Science Ministry Grant No. PGC2018-094626-B-C21 (MCIU/AEI/FEDER, EU) and Basque Government Grant No. IT979-16. M.G.V. and M.I. acknowledge support from the Spanish Ministerio de Ciencia e Innovacion (Grants No. PID2019-109905GB-C21 and No. PGC2018-094626-B-C21) and Basque Government (Grant No. IT979-16). H.L. acknowledges the support by the Ministry of Science and Technology (MOST) in Taiwan under Grant No. MOST 109-2112-M-001-014-MY3.

APPENDIX A: SYMMETRY CONSTRAINTS

According to the analysis in main text, a model which hosts the CICE nodal lines requires at least four bands. Now we try to construct a Hamiltonian in SG *Pbam* (No. 55), in which there are four sets of Wyckoff positions, i.e., $2a$, $2b$, $2c$, and $2d$. Each of them contains two sublattices (denoted by A and B). Thus, to construct a four-band minimal model, two orbitals from each sublattice are required.

The coordinates of the two sublattices for each set of Wyckoff positions are listed here. $2a$: $(0, 0, 0)$, $(\frac{1}{2}, \frac{1}{2}, 0)$; $2b$: $(0, 0, \frac{1}{2})$, $(\frac{1}{2}, \frac{1}{2}, \frac{1}{2})$; $2c$: $(\frac{1}{2}, 0, 0)$, $(0, \frac{1}{2}, 0)$; $2d$: $(\frac{1}{2}, 0, \frac{1}{2})$, $(0, \frac{1}{2}, \frac{1}{2})$. One can find that for any set of Wyckoff positions, sublattice A (B) maps to A (B) under the mirror symmetry \mathcal{M}_z , or inversion symmetry \mathcal{I} . That indicates that the constraints of both \mathcal{M}_z and \mathcal{I} should be written as τ_0 (identity matrix) employing the basis $(A, B)^T$, and the eigenvalue can only be the single value 1. Therefore, the two orbitals selected should carry opposite parity and eigenvalues of \mathcal{M}_z , so that the nodal line band crossings in the (001) plane are protected due to the opposite eigenvalues of mirror symmetry. Indeed, the choices of the Wyckoff positions or orbitals are not unique, e.g., (s, p_z) , (p_x, d_{yz}) , and (p_y, d_{xz}) .

Here we choose two sublattices denoted by A and B occupying the $2a$ Wyckoff position at $\mathbf{r}_A = (0, 0, 0)$ and $\mathbf{r}_B = (\frac{1}{2}, \frac{1}{2}, 0)$ in a unit cell, and each sublattice has two electrons of orbitals p_z and d_{xy} . Employing the basis $\Psi = (p_z^A, d_{xy}^A, p_z^B, d_{xy}^B)^T$, the symmetry constraints at TRIM points take the form

$$\begin{aligned} \Gamma = (0, 0, 0) \cup Z = (0, 0, \pi) : \quad & \mathcal{T} = \mathcal{K}, \quad \mathcal{I} = -\sigma_3, \quad \mathcal{M}_z = -\sigma_3, \quad \mathcal{G}_x = e^{-iq_y/2} \tau_1 \sigma_3, \quad \mathcal{G}_y = e^{-iq_x/2} \tau_1 \sigma_3, \\ S = (\pi, \pi, 0) \cup R = (\pi, \pi, \pi) : \quad & \mathcal{T} = \mathcal{K}, \quad \mathcal{I} = -\sigma_3, \quad \mathcal{M}_z = -\sigma_3, \quad \mathcal{G}_x = -e^{-iq_y/2} i \tau_2 \sigma_3, \quad \mathcal{G}_y = -e^{-iq_x/2} i \tau_2 \sigma_3, \\ X = (\pi, 0, 0) \cup U = (\pi, 0, \pi) : \quad & \mathcal{T} = \tau_3 \mathcal{K}, \quad \mathcal{I} = -\tau_3 \sigma_3, \quad \mathcal{M}_z = -\sigma_3, \quad \mathcal{G}_x = e^{-iq_y/2} \tau_2 \sigma_3, \quad \mathcal{G}_y = -e^{-iq_x/2} i \tau_1 \sigma_3, \\ Y = (0, \pi, 0) \cup T = (0, \pi, \pi) : \quad & \mathcal{T} = \tau_3 \mathcal{K}, \quad \mathcal{I} = -\tau_3 \sigma_3, \quad \mathcal{M}_z = -\sigma_3, \quad \mathcal{G}_x = -e^{-iq_y/2} i \tau_1 \sigma_3, \quad \mathcal{G}_y = e^{-iq_x/2} \tau_2 \sigma_3, \end{aligned} \quad (A1)$$

where $q_{x,y}$ is the k vector from the corresponding TRIM point, Pauli matrices τ and σ are used for the sublattice and orbital space, respectively, and \mathcal{K} is the complex conjugate operator. Given these constraints, the minimal tight-binding model can be constructed.

APPENDIX B: THE ZAK PHASE

The Zak phase γ has been used for the \mathbb{Z}_2 classification of inversion-symmetric 1D insulators, where it can be quantized to 0 or π (mod 2π). It can be also applied to the effective

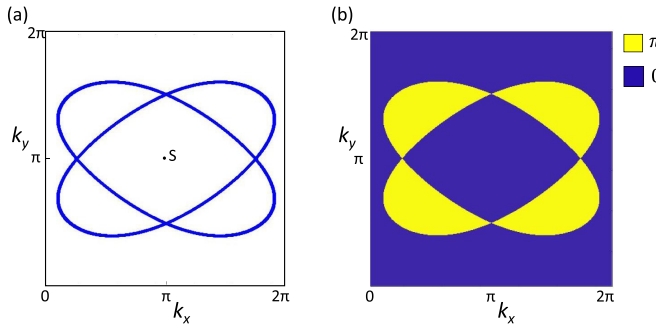


FIG. 4. (a) CICE nodal lines around the S point on the $k_z = 0$ plane. (b) The Zak phase γ distributions for the model. The yellow (blue) color represents π (0). Outside the projection of the NLs, no surface modes can be observed and the Zak phase $\gamma = 0$, while within the area labeled in yellow, there is one DSS. However, within the overlapping area of the projections of two NLs, the Zak phase is 0 (mod 2π), although there are two DSSs within that area, which cannot be characterized by the \mathbb{Z}_2 Zak phase.

1D models along one direction by fixing one or two momenta of 2D or 3D Hamiltonians. In this \mathbb{Z}_2 classification, the bulk-boundary correspondence states that the nontrivial Zak phase $\gamma = \pi$ indicates the emergence of boundary modes, while $\gamma = 0$ is considered a trivial insulator without surface modes. In our model, the CICE NLs consisting of two ellipses lie on the $k_z = 0$ plane. Considering k_x and k_y as parameters, we calculate the Zak phase of the 1D model along the k_z direction, and the CICE NLs are projected on the (k_x, k_y) plane [Fig. 4(a)]. Within the areas of the projection of each one single nodal line, the Zak phase is π , indicating the emergence of one DSS [area labeled in yellow in Fig. 4(b)]. However, within the overlapping area of the projections of two NLs, the Zak phase is 0 [Fig. 4(b)], although there are two copies of DSSs. This implies that the even number of DSSs cannot be characterized by the Zak phase, and is invisible in the \mathbb{Z}_2 classification.

APPENDIX C: OTHER MATERIAL CANDIDATES

We propose CYB_2 [51] and Al_2Y_3 [52] as materials candidates to host CICEs. The crystal structure of CYB_2 is tetragonal with SG $P4_2/mbc$ (No. 135) and shows a layered structure of Y layers intercalated with B and C nets. Al_2Y_3 crystal structure belongs to the $P4_2/mnm$ (No. 136) tetragonal SG. Figures 5(a) and 5(c) and 5(b) and 5(d) show the band structure calculation and crystal structure of CYB_2 and Al_2Y_3 , respectively. The band structures include two essential high-symmetry paths $X \rightarrow \Gamma \rightarrow M$, where the crossings of CICEs are highlighted by black dots. These band structures were calculated using VASP with the modified Becke-Johnson exchange potential in combination with generalized gradient approximation (GGA) [53,54]. The BZ was sampled with a $7 \times 7 \times 9$ Monkhorst-Pack grid and an energy cutoff of 520 eV was used.

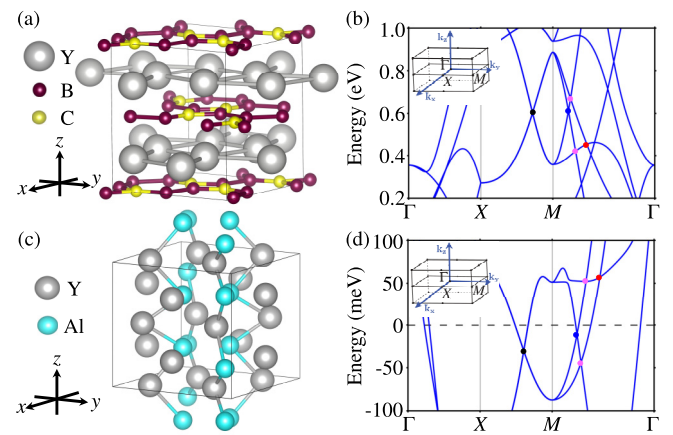


FIG. 5. Crystal structure of bulk (a) CYB_2 with tetragonal SG $P4_2/mbc$ (No. 135) and (c) Al_2Y_3 with tetragonal SG $P4/mbm$ (No. 136). Band structure of (b) CYB_2 and (d) Al_2Y_3 close to the Fermi energy without SOC along the symmetry lines in the Brillouin zone shown in the insets where high-symmetry points are marked. The relevant crossings on $M-\Gamma$ for the half-filling and the second pair of CICEs are indicated by [red, blue] and magenta dots, respectively. The black dots along $X-M$ are the FDPs.

APPENDIX D: DETAILS OF THE CALCULATIONS

In the DFT calculations of ZrAs_2 and ZrP_2 the Perdew-Burke-Ernzherhof [55] implementation of the GGA was used for the exchange-correlation functional. A plane-wave basis with an energy cutoff of 340 eV was employed in all calculations. The BZ was sampled with an $8 \times 15 \times 6$ Monkhorst-Pack grid [56]. The systems were allowed to fully relax until residual atomic forces became smaller than 0.01 eV/Å.

Turning on the SOC in ZrAs_2 opens a small gap of about 8 meV of the band crossings around the U point. Furthermore, we have carried out electronic structure calculations using the modified Becke-Johnson local density approximation (MB-JLDA) exchange-correlation functional which predicts band gaps, effective masses, and frontier-band ordering that are in good agreement with the computationally more intense GW and hybrid functional approaches [57]. The calculations reveal that the band crossings around the U point in ZrAs_2 disappear indicating that the CICEs (and the closing of the gap) is very sensitive to the exchange-correlation functional employed.

A Wannier-function based model for ZrAs_2 and ZrP_2 was obtained using the DFT results as the starting point. The WANNIER90 package along with its interface with the VASP package were employed for this purpose [41]. The upper limit of the frozen energy window was set to 2.5 eV above the Fermi level of each compound. The model perfectly reproduces the DFT bands up to that energy, which is well above the studied band crossings. We chose the following atomic orbitals as the starting guess for the projection of the Bloch states onto Wannier functions: s , p , and d orbitals for Zr and s and p orbitals for As or P.

[1] C. Fang, Y. Chen, H.-Y. Kee, and L. Fu, *Phys. Rev. B* **92**, 081201(R) (2015).

[2] C. Fang, H. Weng, X. Dai, and Z. Fang, *Chin. Phys. B* **25**, 117106 (2016).

[3] H. Weng, X. Dai, and Z. Fang, *J. Phys.: Condens. Matter* **28**, 303001 (2016).

[4] N. P. Armitage, E. J. Mele, and A. Vishwanath, *Rev. Mod. Phys.* **90**, 015001 (2018).

[5] X. Wan, A. M. Turner, A. Vishwanath, and S. Y. Savrasov, *Phys. Rev. B* **83**, 205101 (2011).

[6] A. A. Burkov and L. Balents, *Phys. Rev. Lett.* **107**, 127205 (2011).

[7] S. M. Young, S. Zaheer, J. C. Y. Teo, C. L. Kane, E. J. Mele, and A. M. Rappe, *Phys. Rev. Lett.* **108**, 140405 (2012).

[8] Z. Wang, Y. Sun, X. Q. Chen, C. Franchini, G. Xu, H. Weng, X. Dai, and Z. Fang, *Phys. Rev. B* **85**, 195320 (2012).

[9] S. M. Young and C. L. Kane, *Phys. Rev. Lett.* **115**, 126803 (2015).

[10] T.-R. Chang, S.-Y. Xu, D. S. Sanchez, W.-F. Tsai, S.-M. Huang, G. Chang, C.-H. Hsu, G. Bian, I. Belopolski, Z.-M. Yu *et al.*, *Phys. Rev. Lett.* **119**, 026404 (2017).

[11] W. C. Yu, X. Zhou, F.-C. Chuang, S. A. Yang, H. Lin, and A. Bansil, *Phys. Rev. Mater.* **2**, 051201(R) (2018).

[12] A. A. Burkov, M. D. Hook, and L. Balents, *Phys. Rev. B* **84**, 235126 (2011).

[13] S.-Y. Xu, I. Belopolski, N. Alidoust, M. Neupane, G. Bian, C. Zhang, R. Sankar, G. Chang, Z. Yuan, C.-C. Lee *et al.*, *Science* **349**, 613 (2015).

[14] G. Bian, T.-R. Chang, H. Zheng, S. Velury, S.-Y. Xu, T. Neupert, C.-K. Chiu, S.-M. Huang, D. S. Sanchez *et al.*, *Phys. Rev. B* **93**, 121113(R) (2016).

[15] A. A. Burkov, *Phys. Rev. Lett.* **113**, 247203 (2014).

[16] C.-L. Zhang, S.-Y. Xu, I. Belopolski, Z. Yuan, Z. Lin, B. Tong, G. Bian, N. Alidoust, C.-C. Lee, S.-M. Huang *et al.*, *Nat. Commun.* **7**, 10735 (2016).

[17] J. Hu, S.-Y. Xu, N. Ni, and Z. Mao, *Annu. Rev. Mater. Res.* **49**, 207 (2019).

[18] T. Bzdušek, Q. S. Wu, A. Rüegg, M. Sigrist, and A. A. Soluyanov, *Nature (London)* **538**, 75 (2016).

[19] G. Chang, S. Y. Xu, X. Zhou, S. M. Huang, B. Singh, B. Wang, I. Belopolski, J. Yin, S. Zhang, A. Bansil *et al.*, *Phys. Rev. Lett.* **119**, 156401 (2017).

[20] Z. Yan, R. Bi, H. Shen, L. Lu, S. C. Zhang, and Z. Wang, *Phys. Rev. B* **96**, 041103(R) (2017).

[21] R. Bi, Z. Yan, L. Lu, and Z. Wang, *Phys. Rev. B* **96**, 201305(R) (2017).

[22] B.-J. Yang and N. Nagaosa, *Nat. Commun.* **5**, 4898 (2014).

[23] Z. Gao, M. Hua, H. Zhang, and X. Zhang, *Phys. Rev. B* **93**, 205109 (2016).

[24] B. J. Wieder, Y. Kim, A. M. Rappe, and C. L. Kane, *Phys. Rev. Lett.* **116**, 186402 (2016).

[25] Z. Zhu, G. W. Winkler, Q. S. Wu, J. Li, and A. A. Soluyanov, *Phys. Rev. X* **6**, 031003 (2016).

[26] C. Gong, Y. Xie, Y. Chen, H.-S. Kim, and D. Vanderbilt, *Phys. Rev. Lett.* **120**, 106403 (2018).

[27] S. Ahn, E. J. Mele, and H. Min, *Phys. Rev. Lett.* **119**, 147402 (2017).

[28] Y. Shao, Z. Sun, Y. Wang, C. Xu, R. Sankar, A. J. Breindel, C. Cao, M. M. Fogler, A. J. Millis, F. Chou *et al.*, *Proc. Natl. Acad. Sci. USA* **116**, 1168 (2019).

[29] Z. Wang, A. Alexandradinata, R. J. Cava, and B. A. Bernevig, *Nature (London)* **532**, 189 (2016).

[30] G. Kresse and J. Hafner, *Phys. Rev. B* **48**, 13115 (1993).

[31] P. Blaha, K. Schwarz, F. Tran, R. Laskowski, G. K. H. Madsen, and L. D. Marks, *J. Chem. Phys.* **152**, 074101 (2020).

[32] <https://www.topologicalquantumchemistry.org/>.

[33] B. Bradlyn, L. Elcoro, J. Cano, M. G. Vergniory, Z. Wang, C. Felser, M. I. Aroyo, and B. A. Bernevig, *Nature (London)* **547**, 298 (2017).

[34] M. G. Vergniory, L. Elcoro, C. Felser, N. Regnault, B. A. Bernevig, and Z. Wang, *Nature (London)* **566**, 480 (2019).

[35] T. Zhang, Y. Jiang, Z. Song, H. Huang, Y. He, Z. Fang, H. Weng, and C. Fang, *Nature (London)* **566**, 475 (2019).

[36] F. Tang, H. C. Po, A. Vishwanath, and X. Wan, *Nature (London)* **566**, 486 (2019).

[37] W. Trzebiatowski, S. Weglowski, and L. Lukaszewicz, *Roczn. Chem.* **32**, 189 (1958).

[38] P. E. Blanchard, R. G. Cavell, and A. Mar, *J. Alloys Compd.* **505**, 17 (2010).

[39] R. Marsh, *J. Solid State Chem.* **87**, 467 (1990).

[40] A. Abba Toure, G. Kra, R. Eholie, J. Olivier Fourcade, J. Jumas, and M. Maurin, *J. Solid State Chem.* **84**, 245 (1990).

[41] A. A. Mostofi, J. R. Yates, Y.-S. Lee, I. Souza, D. Vanderbilt, and N. Marzari, *Comput. Phys. Commun.* **178**, 685 (2008).

[42] J. Zak, *Phys. Rev. Lett.* **62**, 2747 (1989).

[43] R. D. King-Smith and D. Vanderbilt, *Phys. Rev. B* **47**, 1651 (1993).

[44] D. Vanderbilt and R. D. King-Smith, *Phys. Rev. B* **48**, 4442 (1993).

[45] S. Ryu and Y. Hatsugai, *Phys. Rev. B* **73**, 245115 (2006).

[46] T. Kariyado and Y. Hatsugai, *Phys. Rev. B* **88**, 245126 (2013).

[47] F. Grusdt, M. Höning, and M. Fleischhauer, *Phys. Rev. Lett.* **110**, 260405 (2013).

[48] R. Barnett, *Phys. Rev. A* **88**, 063631 (2013).

[49] Y.-H. Chan, C.-K. Chiu, M. Y. Chou, and A. P. Schnyder, *Phys. Rev. B* **93**, 205132 (2016).

[50] X. Zhou, C.-H. Hsu, C.-Y. Huang, M. Iraola, J. L. Mañes, M. G. Vergniory, H. Lin, and N. Kioussis, [arXiv:2005.06071](https://arxiv.org/abs/2005.06071).

[51] J. Bauer and J. Debuigne, *J. Inorg. Nucl. Chem.* **37**, 2473 (1975).

[52] T. Dagerhamn, *Ark. Kemi* **27**, 363 (1967).

[53] A. D. Becke and E. R. Johnson, *J. Chem. Phys.* **124**, 221101 (2006).

[54] F. Tran and P. Blaha, *Phys. Rev. Lett.* **102**, 226401 (2009).

[55] J. P. Perdew, K. Burke, and M. Ernzerhof, *Phys. Rev. Lett.* **77**, 3865 (1996).

[56] H. J. Monkhorst and J. D. Pack, *Phys. Rev. B* **13**, 5188 (1976).

[57] Y.-S. Kim, M. Marsman, G. Kresse, F. Tran, and P. Blaha, *Phys. Rev. B* **82**, 205212 (2010).